nature communications

Article

https://doi.org/10.1038/s41467-023-43866-z

Synthesizing evidence for the external cycling of NO_x in high- to low-NO_x atmospheres

Received: 12 April 2023

Accepted: 22 November 2023

Chunxiang Ye[1] ✉, Xianliang Zhou[2,3], Yingjie Zhang[1,4], Youfeng Wang[1], Jianshu Wang[1], Chong Zhang[1], Robert Woodward-Massey[1,5], Christopher Cantrell[6], Roy L. Mauldin III[7,8,9], Teresa Campos[10], Rebecca S. Hornbrook[10], John Ortega[10], Eric C. Apel[10], Julie Haggerty[10], Samuel Hall[10], Kirk Ullmann[10], Andrew Weinheimer[10], Jochen Stutz[11], Thomas Karl[12], James N. Smith[13], Alex Guenther[13] & Shaojie Song[14]

External cycling regenerating nitrogen oxides ($NO_x \equiv NO + NO_2$) from their oxidative reservoir, NO_z, is proposed to reshape the temporal–spatial distribution of NO_x and consequently hydroxyl radical (OH), the most important oxidant in the atmosphere. Here we verify the in situ external cycling of NO_x in various environments with nitrous acid (HONO) as an intermediate based on synthesized field evidence collected onboard aircraft platform at daytime. External cycling helps to reconcile stubborn underestimation on observed ratios of $HONO/NO_2$ and NO_2/NO_z by current chemical model schemes and rationalize atypical diurnal concentration profiles of HONO and NO_2 lacking noontime valleys specially observed in low-NO_x atmospheres. Perturbation on the budget of HONO and NO_x by external cycling is also found to increase as NO_x concentration decreases. Consequently, model underestimation of OH observations by up to 41% in low NO_x atmospheres is attributed to the omission of external cycling in models.

Nitrogen oxides ($NO_x \equiv NO + NO_2$) and gaseous nitrous acid (HONO) perturb the photochemical cycling of peroxy radicals (RO_2 and HO_2) and hydroxide radicals (OH)[1–6]. Field observations in high-NO_x atmospheres highlight the primary production of OH (and NO) via HONO photolysis[1,6–10]. Across high- to low-NO_x atmospheres, secondary production of OH via the HO_2 plus NO reaction is another major source of OH.

HONO and NO_x are closely coupled in their NO_x-HONO internal cycling, referred to as internal cycling in this context (Fig. 1). Specifically, heterogeneous reactions of NO_2 on ambient surfaces and

---

[1]State Key Joint Laboratory of Environmental Simulation and Pollution Control (SKL-ESPC), College of Environmental Sciences and Engineering, Peking University, Beijing, China. [2]Wadsworth Center, New York State Department of Health, Albany, NY, USA. [3]Department of Environmental Health Sciences, State University of New York, Albany, NY, USA. [4]School of Ecology and Nature Conservation, Beijing Forestry University, Beijing, China. [5]Department of Chemistry, University of Leeds, Leeds, UK. [6]Université Paris-est Créteil, LISA (Laboratoire Interuniversitaire des Systèmes Atmosphériques), Paris, France. [7]Center for Atmospheric Particle Studies, Carnegie Mellon University, Pittsburgh, PA, USA. [8]Department of Chemistry, Carnegie Mellon University, Pittsburgh, PA, USA. [9]Department of Atmospheric and Oceanic Sciences, University of Colorado Boulder, Boulder, CO, USA. [10]National Center for Atmospheric Research, Boulder, CO, USA. [11]Department of Atmospheric and Oceanic Sciences, University of California, Los Angeles, CA, USA. [12]Institute for Meteorology and Geophysics, University of Innsbruck, Innsbruck, Austria. [13]Earth System Science, University of California, Irvine, CA, USA. [14]State Environmental Protection Key Laboratory of Urban Ambient Air Particulate Matter Pollution Prevention and Control & Tianjin Key Laboratory of Urban Transport Emission Research, College of Environmental Science and Engineering, Nankai University, Tianjin, China. ✉e-mail: c.ye@pku.edu.cn

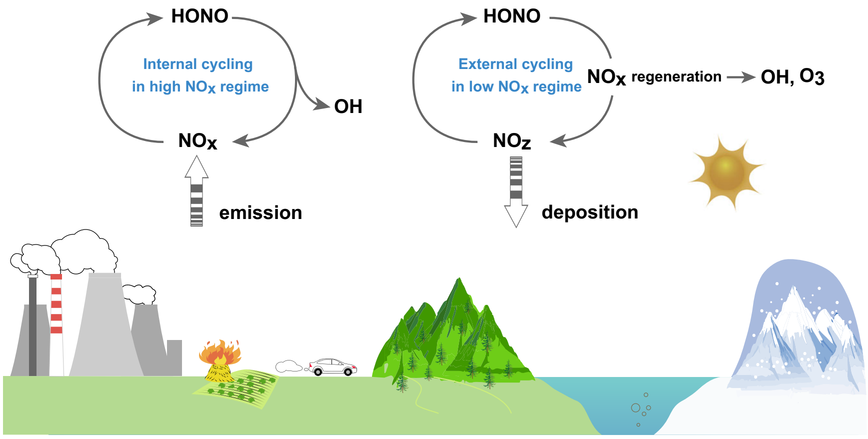

Fig. 1 | Schematic graph of internal cycling and external cycling of NO and HONO. The left reaction scheme describes internal cycling between nitrogen oxides (NO = NO + NO) and nitrous acid (HONO) in high- NO atmospheres. HONO photolysis is the major route producing OH radical (OH). The right reaction scheme describes external cycling among oxidative reservior species of NO (NO), NO, and HONO in low-NO atmospheres. NO -catalysed radical chain propagration takes over as the major route perturbing OH and ozone (O) chemical production.

gas-phase reactions between NO and OH have been intensively examined as major HONO formation routes in the internal cycle[7–15]. Since HONO photolyzes much faster, turnover routes of NO_x to recycle HONO are the rate-limiting steps of internal cycling. OH is a net product in internal cycling even if only HONO production via heterogeneous reactions of NO_2 is considered. Any external source (or sink) of HONO or NO_x would promote (or suppress) the internal cycling. Apart from the internal cycling, NO_x ages to form more oxidized reservoirs, which are referred to as NO_z, as air masses are transported away from source regions. NO_x aging processes suppress the internal cycling and diminish the role of HONO photolysis in the OH budget. However, model underestimation of the NO_x/NO_z ratio observations suggests unknown or underappreciated NO_x regeneration pathways from NO_z in low-NO_x atmospheres[4,16–28]. NO_x regeneration pathways, in contrast to the internal cycling, produce "new" NO_x and hence are designated as the external cycling of NO_x (Fig. 1). External cycling naturally promotes the internal cycling via at least an external source of NO_x. Consequently, secondary OH production via NO_x regeneration and net primary OH production via HONO regeneration could greatly perturb the OH photochemical budget. The current model omission of external cycling would lead to an underestimation of OH production and OH abundance, especially in low-NO_x atmospheres.

Identifying and exploring a specific mechanism is a natural step in characterizing external cycling and quantifying its impact on the oxidative capacity of the atmosphere. The external cycling pathways proposed in the literature include at least three mechanisms, i.e., surface-catalyzed photolysis of absorbed nitrate (nitrate$_{abs}$) on snow/ice surfaces and possibly also on aerosol/ambient surfaces[4,20,24,27–38], nitrification/denitrification in the soil[16,19] and the thermal decomposition of peroxyacetyl nitrate (PAN). Among these mechanisms, surface-catalyzed photolysis of nitrate$_{abs}$ on aerosol surfaces, referred to as pNO_3 photolysis, occurs in situ in the air column and therefore potentially perturbs the distribution of NO_x and hence the oxidative capacity of the atmosphere from the lower troposphere to the upper troposphere[35]. pNO_3 photolysis has been intensively explored in laboratory and field studies[4,18,21–23,34,36,37,39]. The reaction rate constant of pNO_3 photolysis varies over at least two orders of magnitude in high-to low-NO_x atmospheres by employing a budget analysis for either HONO or NO_2 and by assuming that pNO_3 photolysis fully accounts for the missing source of HONO or NO_2 in the field[4,21,32,34,38]. Laboratory studies on a variety of pNO_3 samples have confirmed that pNO_3 photolysis is greatly enhanced compared to that of gaseous HNO_3 and that the pNO_3 photolysis rate constant is highly variable, over 3 orders of magnitude[30,36,37] Based on these laboratory and field studies, Ye et al. and Andersen et al. have also revealed that pNO_3 photolysis is surface-catalyzed in nature and is greatly affected by the physicochemical properties of aerosol particles, such as pNO_3 loading, chemical composition and particle size[30,38]. Efforts in characterizing atmospheric aerosol properties and their photochemical reactivities are critical in quantitatively understanding the role of pNO_3 photolysis in external cycling. However, the limited availability of the pNO_3 photolysis rate constant in only a few atmospheric environments, its large variability, and potentially large uncertainties make it difficult to extrapolate results from laboratory studies to field studies or directly compare results among field studies[18,21,22,30,33,34,36–39]. The variability and potentially large uncertainties in the rate constant have also precluded as yet confident confirmation of pNO_3 photolysis or other reactions as the dominant mechanism of the external cycling or direct characterization of the external cycling in the atmosphere. To solve this dilemma, we suggest synthesizing critical observational and model evidence, summarizing the fundamental characteristics, and quantifying the impact of the external cycling on the oxidative capacity of the atmosphere in high- to low-NO_x atmospheres through a broader lens rather than attempting to establish the kinetics or the dominant mechanism of the external cycling.

Results and discussion

Synthesized field evidence for external cycling

A comprehensive dataset obtained from an aircraft measurement campaign provided excellent insight into the external cycling of NO_x and its perturbation on the oxidative capacity of the atmosphere[4,32]. Nineteen research flights were conducted onboard NSF/NCAR C-130 to collect measurements of NO_x, HONO, nitric acid (HNO_3), particulate nitrate (pNO_3), some alkyl nitrates, PAN, radicals (OH, HO_2, RO_2), ozone (O_3), volatile organic compounds (VOCs), aerosol size distributions, photolysis frequencies, and other meteorological parameters, mostly in various locations in the low-NO_x troposphere (Methods), i.e., from the pristine terrestrial and marine boundary layer (BL) to the FT (Fig. S1 and Table S1). Herein, we defined low-NO_x and high-NO_x regimes with a NO_x concentration threshold of 500 pptv, given that 500 pptv represented the upper limit concentration of NO_x in the remote troposphere. Furthermore, 500 pptv appeared to be a turning point for the external cycling to be key sources of HONO and NO_x (see below). The data were collected from nineteen research flights without further screening and offered a more global representativity and atmospheric variability of the external cycling and therefore supported our analysis strategy for directly exploring the external cycling of NO_x across high- to low-NO_x atmospheres. In our previous publications, we exploited data from a limited number of research flights in forested areas (i.e., RF4-5, 11, 17-18) and clean marine boundary layers (i.e., RF14, 16) and discussed the budget of HONO and specific mechanism of the external cycling[4,32]. Several studies of this kind based on aircraft observations had generally employed the budget analysis methodology for HONO to conduct case studies in clean marine air or fire plumes[21,34,38]. The reaction rate constant of the specific external cycling route implied from the missing HONO source among these reports deviated by more than two orders of magnitude, reaching no consensus in the dominant external cycling route or atmospheric variability in the external cycling[4,21,32,34,38].

The NO_2 mixing ratios ranged from 10 pptv to 14.2 ppbv, with median values of approximately 30 pptv in the FT and 218 pptv in the BL (Fig. 2 and Table S2). While ppbv levels of NO_2 were occasionally found as we flew through urban and industrial plumes, the median values of both HONO and NO_2 were not affected by these high values and were still representative of the background troposphere. The median NO_2 in the BL and the FT agreed with the established NO_2 distribution in these background atmospheres[5,21,26,38,40–42]. The median HONO mixing ratio was approximately 7.0 pptv in the FT background and 12.1 pptv in the BL background (Fig. 2 and Table S2). Our data provided the first illustrations of the HONO distribution in such a variety of low-NO_x atmospheres. The median HONO in the BL was among the lowest ever reported in specific low-NO_x environments, such as in snow/ice-covered polar areas[20,27–29], pristine terrestrial boundary layers[32,43], and clean marine boundary layers[4,23,25,38]. The median HONO in the FT was slightly lower than values reported from other aircraft observations in low-NO_x atmospheres[41,43] but was one or two orders of magnitude lower than those observed in plumes[34,44].

The GEOS-Chem model was used to provide a benchmark for the concentration ratios among reactive nitrogen species, such as the HONO/NO_y ($\equiv NO_x + NO_z$) ratio, NO_2/NO_y ratio and HONO/NO_2 ratio. The emission inventory applied in GEOS-Chem overestimated NO_x emissions[45]. However, this drawback might not interfere with the model simulation of the HONO/NO_2 ratio and NO_2/NO_y ratio in various low-NO_x air masses since the reactive nitrogen species aged to reach their photosteady state (PSS) in the low-NO_x atmosphere. Even with the anticipated model overestimation of NO_2 and consequently overestimation of NO_z (Fig. S2), the HONO concentration, HONO/NO_y ratio and NO_2/NO_y ratio were substantially underestimated in the model (Fig. 2), indicating the external cycling of NO_x. Moreover, model underestimation of the HONO/NO_2 ratio and HONO/NO_y further revealed that HONO might be an intermediate in the external cycling of NO_x, as HONO regenerated in the external cycling would rapidly photolyze to produce NO_x (Fig. 2). It was speculated that the relatively slow turnover rate of NO_x to produce HONO was associated with a low HONO/NO_2 ratio (<0.05, as commonly observed in high-NO_x atmospheres[9]) to balance the rapid turnover rate of HONO to produce NO_x via HONO photolysis and the Leighton cycle. Herein, a much higher HONO/NO_2 ratio relative to the PSS prediction in GEOS-Chem indicated a net turnover of HONO to produce NO_x in the external cycling and presented HONO as an intermediate product. Nevertheless, direct regeneration of NO_x in the external cycling bypassing HONO intermediate could not be excluded.

The external cycling route of NO_x with NO_z as a precursor and HONO as an intermediate could be proposed based on the synthesized evidence from the concentration ratios of reactive nitrogen species. Anthropogenic emission perturbation, internal cycling mechanisms, and measurement interferences to reconcile the model–observation discrepancies could be safely excluded. First, anthropogenic emissions of HONO and NO_x perturbed the distribution of HONO within a transport height of approximately 300 m while perturbing the distribution of NO_2 within the boundary layer[16,19,32]. The nineteen research flights spent over 85% of the time 600 m above the ground surface in the BL and over 45% of the time in the FT. Hence, anthropogenic emissions of HONO and NO_x could be excluded as the major reason for the model–observation discrepancies in the concentration ratio of reactive nitrogen species. Second, the photosensitization reactions of NO_2 produced HONO, with photo-enhanced rates several-fold higher at noon in low-NO_x conditions than at nighttime in high-NO_x conditions;[7,8,10] however, they were still too slow to account for the high HONO/NO_2 ratio observed (Fig. 2). In fact, fully reconciling model–observation discrepancies in the HONO/NO_2 ratio required a reactive uptake coefficient of NO_2 to produce HONO to be in the order of magnitude of 10^{-3}, which was nearly two orders of magnitude higher than the proposed photo–enhanced values at noon in low-NO_x conditions[7,10]. In addition, such photosensitization reactions were not related to the model–observation discrepancy in the NO_2/NO_y ratio. Finally, a substantially positive measurement interference in HONO coupled with negative measurement interferences in NO_z species, such as HNO_3 and pNO_3, might improve the model–observation agreement for both the HONO/NO_2 ratio and NO_2/NO_y ratio. However, such species-dependent interference was not practical, as any positive (or negative) nitrite anion interference in HONO measurement would also result in a positive (or negative) interference in pNO_3 and HNO_3 measurements. A comparison of our LPAP HONO measurements with those by the DOAS instrument showed reasonable consistency in the concentration range beyond the detection limit of both instruments, but DOAS showed a smaller value relative to LPAP in the lower concentration range[4]. Potential chemical interferences for LPAP HONO, including HNO_4 and particulate nitrite, were not directly measured. PSS HNO_4 interference calculations suggested that it only caused minor interference (<15% of signal)[32]. The low partitioning ratio of particulate nitrite over HONO and low sampling efficiency of particulate nitrite in the LPAP system also suggested minor interferences (<1% of signal)[46–48]. Therefore, our HONO measurement had only been corrected for PSS HNO_4 interference and therefore, the LPAP HONO measurement appeared to be reasonably reliable in our campaign. Measurements of pNO_3 and HNO_3 had not been corrected for PSS HNO_4 interference since the interference was small relative to the signals. Similarly, reliable NO_x measurements have been widely reported in the literature[40]. Although potential positive interference was not totally excluded[49], model underestimation of such as the HONO/NO_2 ratio would be even worse assuming potential positive interference of NO_2. As such, although measurement interferences could not be completely excluded for HONO, NO_x, pNO_3, and HNO_3 measurements, the potential interferences were either very small or did not show the species-dependent characteristics required to reconcile the model–observation discrepancies. These analyses further supported the external cycling as a proper cause to reconcile the model–observation discrepancies.

Helas and Warneck and Ye et al. deduced that the lack of expected daytime minima of NO_2 and HONO might be additional critical evidence for the external cycling, at least for the low-NO_x marine boundary layer[4,26]. Bell-shaped diurnals of HONO and NO_2 were observed as critical evidence for the external cycling powered by snow photochemistry in polar areas[29,50]. Their deduction followed a budget analysis of NO_2 and HONO. The oxidation of NO_2 was a major sink for NO_2, with the rate scaling with the radical concentration or photolysis frequency of O_3 (jO^1D). Additionally, partitioning of NO_2 over NO was also promoted by fast photolysis of NO_2 to produce NO at noon, as determined in the Leighton cycle[40,42]. Both chemical processes contributed to a noontime minimum of NO_2. For HONO, daytime photolysis was the largest budget term and dominated the diurnal profile[1,2]. Therefore, typical U-shaped diurnal profiles for NO_2 and HONO were expected and generally observed in high-NO_x atmospheres[1,2,40,42]. External cycling of NO_2 and HONO might compensate for their daytime losses and result in atypical diurnal profiles of HONO and NO_2, including flat and even bell-shaped profiles depending on the rate of external cycling[4,22,25].

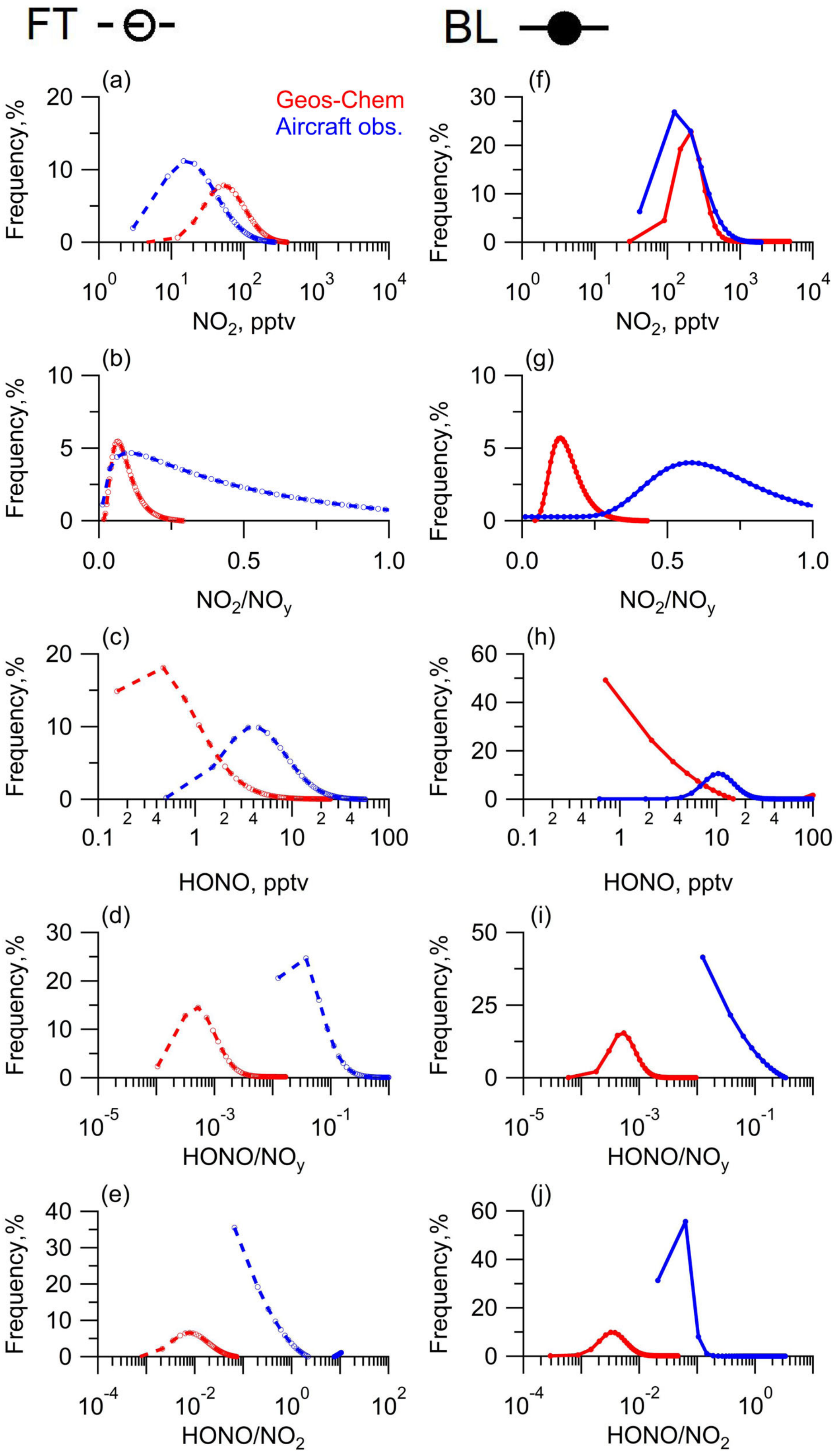

Fig. 2 | Frequency distribution of concentrations and concentration ratios of the reactive nitrogen species as measured onboard the C-130 research aircraft and simulated by GEOS-Chem. a–e Distribution of NO_2 concentration, the concentration ratio of NO_2/NO_y, HONO concentration, the concentration ratio of HONO/NO_y, and the concentration ratio of HONO/NO_2 in the free troposphere (FT), respectively. **f–j** Distribution of NO_2 concentration, the concentration ratio of NO_2/NO_y, HONO concentration, the concentration ratio of HONO/NO_y, and the concentration ratio of HONO/NO_2 in the boundary layer (BL), respectively. The red lines with circles represent the GEOS-Chem model predictions. The blue lines with circles represent our aircraft observations. Open circles and solid circles represent data points from the FT and the BL, respectively. Dashed lines and solid lines connect adjacent data points.

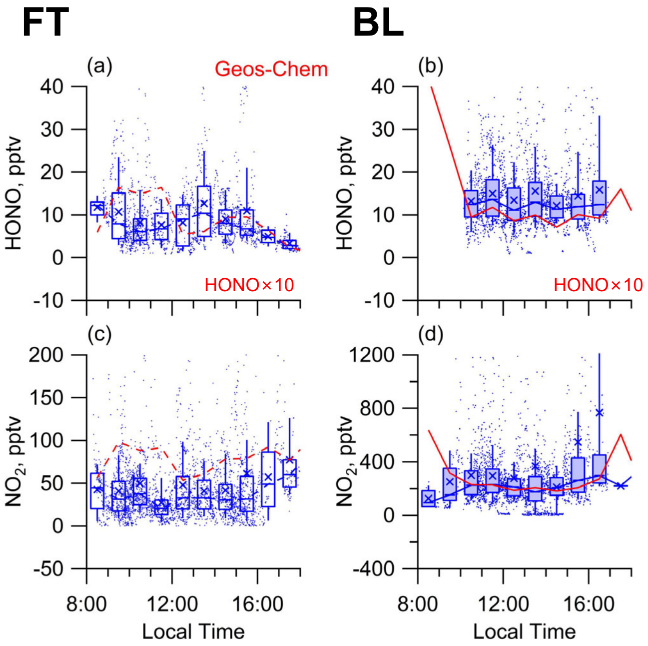

Fig. 3 | Diurnal profiles of HONO and NO_2 as measured onboard the C-130 research aircraft and simulated by GEOS-Chem. a, **b** Diurnal profiles of HONO in the free troposphere (FT) and boundary layer (BL), respectively. **c**, **d** Diurnal profile of NO_2 in the FT and BL, respectively. The red dashed and solid lines represent the median values of the GEOS-Chem model predictions. The blue boxes represent, from top to bottom, the 75th, 50th, and 25th percentiles; the whiskers above and below the boxes represent the 90th and 10th percentiles; and the cross represents the mean value of our aircraft observations. Open boxes and solid boxes represent data points from the FT and the BL, respectively. The blue dashed lines and solid lines connect adjacent median values.

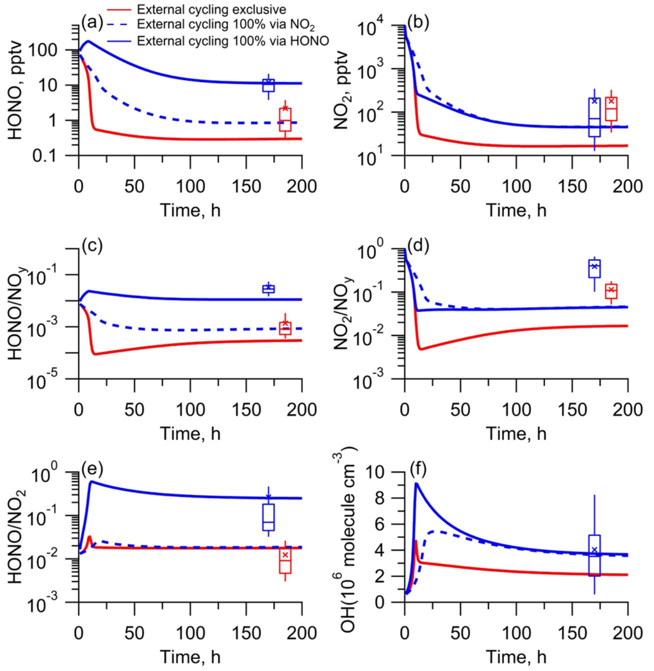

Fig. 4 | Distribution patterns of concentration and concentration ratios of reactive nitrogen species, and OH radicals during plume aging as simulated by the MCM model. a, **b** Concentrations of HONO and NO_2, respectively. **c–e** Concentration ratio of $HONO/NO_y$, NO_2/NO_y, and $HONO/NO_2$, respectively. **f** Concentration of OH radicals. The red line represents the model S0, which excludes external cycling. The blue line and blue dashed line present the model S1 and S2, which include the proxy mechanism for external cycling with HONO yields of 100% (0% yield for NO_2) and 0% (100% yield for NO_2), respectively. The blue and red boxes represent the results of our aircraft observations and GEOS-Chem simulations, respectively. From top to bottom of the box, the 75th, 50th, and 25th percentiles are shown; the whiskers above and below the boxes represent the 90th and 10th percentiles; and the cross represents the mean values.

Although the 19 research flights sampled various airmasses over a large geographic area across a variety of chemical regimes in the atmosphere during different hours of the day, typical photochemical peaks in radicals and jO^1D were still observed (Fig. S3), and therefore the typical diurnals of HONO and NO_2 were expected. However, we observed atypical diurnal profiles that lacked daytime minima of NO_2 and HONO in more general BL, adding to the previous observation of the same kind in the clean marine boundary layer and polar boundary layer and first in the FT (Fig. 3). This observation also differed from the GEOS-Chem simulation which excluded external cycling and simulated the expected diurnal profiles of NO_2 and HONO, especially in the BL (Fig. 3). Therefore, the atypical diurnal profiles of NO_2 and HONO provided further observational evidence of the temporal distribution of reactive nitrogen to verify the external cycling of NO_x and HONO. Notably, neither of the internal cycling mechanisms, such as the photosensitization reaction of NO_2, nor potential measurement interferences of HONO or NO_2, were able to reconcile model–observation discrepancies in the diurnal profiles of NO_2 and HONO.

Chemical model evaluation of external cycling

As the GEOS-Chem did not compile detailed radical chemistry along the oxidation mechanism of VOCs[51,52], a nearly explicit chemical model (MCM version 3.3.1, http://mcm.leeds.ac.uk/MCM/) was adapted to simulate the photochemical evolution of a random power plant plume (Fort Martin station power plant plume captured in RF10, Methods) to represent nitrogen cycling photochemistry across various NO_x regimes over a large geographic area. The objectives of the chemical model simulation were to explore the fundamental characteristics of external cycling (i.e., HONO being an intermediate, determinative role of external cycling in the observed high ratio of $HONO/NO_2$ and NO_2/NO_y, and the perturbation of external cycling on OH photochemistry) along with the aging of the plume. To be more specific, measurements in the power plant plume were chosen to initialize our model, while chemical conditions in the low-NO_x atmosphere were carefully summarized to constrain the model. To focus on the chemical evolution of composition in the plume, a conceptual photochemical evolution under solar noon conditions was simulated in our model. To avoid discussion on any specific external cycling mechanism and related arguments on the reaction rate of specific external cycling routes, a proxy mechanism for the external cycling employing pNO_3 as a representative of NO_z species and the precursor of HONO and NO_x in the external cycling was included in the chemical model scheme. The pNO_3 photolysis rate or the reaction rate of a general NO_z species was set up based on the assumption that the external cycling could fully account for the unknown source of HONO or NO_2. Previous field observations or laboratory measurements of the photolysis rate constant were not referred to or compared with, as only a proxy mechanism, rather than a specific mechanism, of the external cycling was the very core of the discussion. Three independent models were run: one excluded the external cycling of NO_x and HONO (model S0), and the other two included external cycling, with/without HONO as a NO_x intermediate (model S1-S2). Since the external cycling was verified and HONO was identified as an intermediate product based on our observations, chemical model S1 was expected to best represent our observations on the distribution of HONO and NO_2 in varied NO_x regimes.

The kinetic curve of reactive nitrogen species during the aging of the Fort Martin station power plant plume was shown in Fig. 4. NO_2 went through quasi-exponential decay in the initial period and then

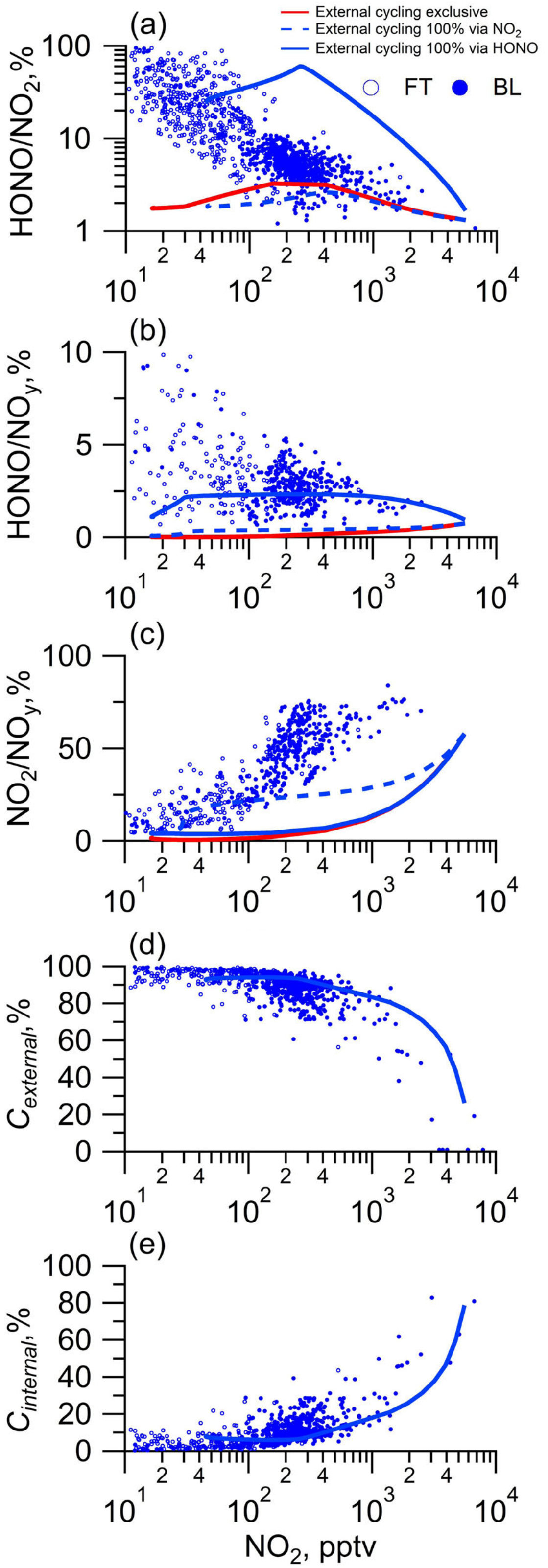

Fig. 5 | Scatter plots of the concentration ratios of reactive nitrogen species, and contribution of external and internal cycling, against NO_2, as measured onboard the C-130 research aircraft and simulated by the MCM model. **a**–**c** Concentration ratios of $HONO/NO_2$, $HONO/NO_y$, NO_2/NO_y, respectively. **d**, **e** External source contribution ($C_{external}$) and internal source contribution ($C_{internal}$), respectively. Open circles and solid circles represent measured data points from the free troposphere (FT) and the boundary layer (BL), respectively. The red line represents model S0, which excludes external cycling. The blue line and blue dashed line present the model S1 and S2, which include the proxy mechanism for external cycling with HONO yields of 100% (0% yield for NO_2) and 0% (100% yield for NO_2), respectively.

approached a steady period with a stabilized NO_2/NO_y ratio and any other concentration ratios of reactive nitrogen species (Fig. 4). The initial period simulated reactive nitrogen photochemistry in a fresh plume or high-NO_x atmosphere where the oxidation of NO_x to form NO_z species dominated the NO_x budget, leading to rapid NO_2 decay. The steady period mimicked reactive nitrogen photochemistry in aged plumes or in low-NO_x atmospheres where the oxidation loss and regeneration of NO_2 from the external cycling approached an equilibrium state, resulting in relatively consistent NO_2 levels that had been persistently observed in various low-NO_x atmospheres in our study and in the literature[4,21,40].

The counterbalancing role of NO_x regeneration in the external cycling extended the NO_x lifetime and sustained comparable NO_x abundance in aged airmasses or remote atmospheres. It also challenged the current chemical model scheme involving the continuous oxidative decay of NO_x and a small NO_x regeneration rate, leading to extremely low NO_x abundance in the tropospheric background. In model S0, the NO_2/NO_y ratio was not negligible but was extremely low (Fig. 4) due to the low regeneration rate of NO_x via transport and the thermal decomposition of PAN, even with higher PAN and higher rates of PAN decomposition applied in the model than those obtained from our aircraft observations (Fig. S4). The external cycling of NO_x in model S1 or S2 better agreed with the observed NO_2 concentrations and concentration ratios of NO_2/NO_y in low-NO_x environments, confirming the determinative role of the external cycling in the distribution of NO_2/NO_y ratio especially in low-NO_x atmospheres. Model S1 also better agreed with the HONO concentration, $HONO/NO_y$ ratio, and $HONO/NO_2$ ratio, confirming HONO as an intermediate in the external cycling. Compared to other NO_x regeneration mechanisms, such as thermal decomposition and photolysis of PAN (gaseous HNO_4, organic nitrates, and nitric acid), the external cycling involving HONO as an intermediate proceeded far more rapidly, especially in low-NO_x atmospheres.

To note, our observation and modeling consistently demonstrated the environmental variability pattern in the role of external cycling as the plume aged, and our modeling with the external cycling better captured the observed ratios of $HONO/NO_2$, $HONO/NO_y$, NO_2/NO_y as NO_x decreased (Fig. 5). These environmental variability patterns were mainly rationalized by the accumulation of NO_z (the external cycling precursor) as the plume aged. Consequently, an increasing trend in the $HONO/NO_2$, $HONO/NO_y$ ratio and therefore a relatively strong external cycling contribution ($C_{external}$) to the budget of HONO and NO_x as NO_x decreased were observed (see Calculation of $C_{internal}$ and $C_{external}$ in Method section). The environmental variability of the rate constant of the external cycling, i.e., the high rate constant of the external cycling in low NO_x atmospheres, might also contribute to the environmental variability patterns[30]. Although the environmental variability in the rate constant of the external cycling was not considered in our box model scheme, our model reasonably captured the observations across NO_x regimes. Therefore, both our observations and the model simulation illustrated increasing perturbations on atmospheric budgets of reactive nitrogen species by the external cycling as NO_x decreased.

Frankly speaking, it is difficult to comprehend the observed trend of $C_{external}$ as NO_x decreases since it goes against the traditional theories in which internal cycling dominates the HONO budget. The shifting of the $HONO/NO_2$ ratio as NO_x decreased in the high-NO_x atmosphere was so slow and limited in a narrow range, typically from 0.01 to 0.1 (Figs. 4, 5), that it might have been considered unchanged given the observational uncertainties. The relationship between HONO and NO_x was strengthened by numerous observations in high-NO_x

atmospheres[1,9,13], and the dominant role of the internal cycling tended to be mistakenly extrapolated to low-NO_x chemical regimes as a consequence. Our characterization of the chemical-regime-dependent contribution of the external cycling better summarized the environmental variability feature of the external cycling and properly addressed the observational argument regarding missing HONO sources in high-NO_x atmospheres and low-NO_x atmospheres[44].

The increasing contribution of the external cycling to the budget of HONO and NO_x as NO_x decreased might have amplified its perturbation on OH photochemistry because OH production was mostly sensitive to the abundance shifting of NO_x in the low-NO_x atmosphere. In addition, the daytime compensation of NO_x by the external cycling might have further amplified its perturbation role because the photochemical production of OH overlapped with the external cycling of NO_x and HONO during the daytime. This point was illustrated in the model underestimation of OH. Due to model S0 omission of the external cycling, the model underestimated OH, and this underestimation was more apparent in a low-NO_x atmosphere than in a high-NO_x atmosphere (Fig. 4). The model underestimation of OH was also confirmed to be more closely linked with primary OH production via photolysis of HONO (driven mainly by the internal cycling) in a high-NO_x atmosphere but more closely associated with NO_x-catalyzed secondary OH production driven by the external cycling of NO_x in a low-NO_x atmosphere. The S0 model underestimation of OH abundance reached approximately 41% in a low-NO_x atmosphere (Fig. 4), comparable to a previous CTM evaluation, which showed a perturbation of the NO_x budget and therefore the OH budget by approximately 40% via a proxy cycling mechanism in the marine boundary layer[35].

Overall, the results of our analysis indicate the dominant role of external cycling in the chemical budget of reactive nitrogen in low-NO_x atmospheres and its significant impact on oxidant photochemistry, thus calling for an urgent and significant revision in our understanding of the atmospheric chemistry of reactive nitrogen and oxidants. To advance this goal, extensive research efforts are needed, for example, laboratory work to better parameterize the kinetics and mechanisms of dominant external cycling routes, including but not limited to pNO_3 photolysis, and field measurements to establish spatial and temporal distributions of reactive nitrogen species that are only sporadically available at this time, especially for low-NO_x atmospheres[5,17,34,53,54].

Methods

Aircraft observation

A total of 19 research flights were conducted, mostly from 8:00 to 18:00 local time, in various low-NO_x troposphere environments. The raw data from the first 15 min after taking off and the last 15 min before landing were excluded from the analysis to avoid interference from pollution at the airport and were then averaged for 3 min for further analysis.

O_3 and NO_x were measured using chemiluminescence methods[55,56]. HONO, HNO_3, and pNO_3 were measured using a wet-chemistry method similar to LOPAP[57]. Aerosol number-size distributions were measured using a scanning mobility particle sizer (SMPS) and an ultrahigh sensitivity aerosol spectrometer (UHSAS)[58]. Alkyl nitrates, PANs, and VOCs were measured by a trace organic gas analyzer (TOGA)[59]. Free radicals were measured using a selected-ion chemical-ionization mass spectrometer (SICIMS)[60]. Photolysis frequencies were calculated from measurements of a scanning actinic flux spectroradiometer (SAFS)[61].

Calculation of $C_{internal}$ and $C_{external}$

The internal cycling included heterogeneous reactions of NO_2 on ambient surfaces, gas-phase reaction between NO and OH radicals, HONO photolysis, and gas-phase reaction between HONO and OH radicals. The chemical reactions are listed as follows.

$$NO_2 + \text{surface} \rightarrow HONO + \text{other products}$$

$$HONO + h\upsilon\,(\lambda < 400\text{nm}) \leftrightarrow OH + NO$$

$$HONO + OH \rightarrow H_2O + NO_2$$

The internal source of HONO ($P_{internal}$) is calculated with the equation below:

$$P_{internal} = k_{R1}\left[NO_2\right] + k_{R2}[OH][NO] \quad (1)$$

where [X] represents the concentration of species X in molecule cm^{-3}; k_{R2} is the rate constant of NO with OH radicals; k_{R1} is defined as the heterogeneous uptake rate constant of NO_2 on the aerosol surface and is calculated with Eq. (2).

$$k_{R2} = \frac{1}{4} \times s/\upsilon \times c \times \gamma \quad (2)$$

where s/υ represents the aerosol surface density, which is calculated from the particle number-size distribution by the SMPS. c represents the average molecular speed of NO_2. γ represents the uptake coefficient of NO_2 on an aerosol particle surface. An upper limit of 10^{-4} was adopted to estimate the upper limit of internal sources of HONO[62].

With a photolytic lifetime of approximately 10 min, the photosteady-state assumption is applicable for HONO. The external source of HONO ($P_{external}$) is calculated according to the photosteady-state budget as follows.

$$P_{internal} + P_{external} = (j_{HONO} + k_{R3}[OH]) \times [HONO] \quad (3)$$

where [X] represents the concentration of species X in molecule cm^{-3}, j_{HONO} represents the photolysis frequency of HONO, and k_{R3} represents the rate constant of HONO with OH radicals. Soil and anthropogenic emissions of HONO are not included in the budget. The aircraft measurements were mostly taken ≥ 600 m above the ground in the boundary layer and up to 8000 m in the free troposphere. The air masses encountered were therefore decoupled from ground surface HONO sources such as soil emissions and heterogeneous reactions of NO_2 at ground surfaces[63]. The high HONO/NO_2 ratio observed here also excluded influences from primary HONO emissions except for occasional influences from power plant plumes or city plumes. Therefore, only in situ chemical reactions were considered for the internal and external cycling rate calculation in this study.

The relative contribution of the internal source and external source to the total HONO source, $C_{internal}$ and $C_{external}$, can be defined as follows:

$$C_{internal} = \frac{P_{internal}}{P_{internal} + P_{external}} \quad (4)$$

$$C_{external} = \frac{P_{external}}{P_{internal} + P_{external}} \quad (5)$$

Nearly explicit chemical model simulation

The master chemical mechanism (MCM v3.3.1) is adapted here to simulate nitrogen cycling photochemistry and its impacts on the oxidative capacity of the atmosphere. The specific objective of the model run was to test whether the external cycling proxy mechanism, i.e., particulate nitrate photolysis or reaction of a general NO_z species, can reproduce the unique distribution patterns of OH, HONO, and NO_2 in the low-NO_x troposphere.

The chemical scheme extracted from the MCM website was employed. The initial mechanism revisions of the MCM model include the addition of the heterogeneous production of HONO from NO_2 reactions, dry deposition-driven removal of model-calculated OVOC intermediates and reactive nitrogen species, and a transport source for HNO_3 and PAN to compensate for dry deposition losses of NO_y species[22,25]. The conversion rate of HONO from NO_2 reactions is set to be $1.4 \times 10^{-5} s^{-1}$ ($\sim 0.05 h^{-1}$). The dry deposition-driven removal of model-calculated OVOC intermediates and reactive nitrogen species are set to be $9.0 \times 10^{-6} s^{-1}$ and $1.0 \times 10^{-5} s^{-1}$, respectively. Both the transport source rate for HNO_3 and PAN are 18 pptv h^{-1}. This model mechanism setup is referred to as the baseline model, S0, which excludes the external cycling proxy mechanism. In further revised models (model S1 and S2), we added HONO production from the proxy mechanism of the external cycling (Table S3). The production rate of HONO or NO_2 (P_{pNO_3}) was expressed as follows:

$$P_{pNO_3} = [pNO_3] \times j_{HNO3} \times EF \tag{6}$$

where j_{HNO3} is the photolysis frequency of HNO_3 in its gaseous form, and the enhancement factor, *EF*, is the ratio of the photolysis rate constant of particulate nitrate relative to j_{HNO3}. A median *EF* of 150 and a $pNO_3/tHNO_3$ partitioning ratio of 0.5 were employed in the model to represent the average conditions for the background troposphere[30]. A HONO yield of 100% (S1, 0% yield for NO_2) or 0% (S2, 100% yield for NO_2) was adapted in models S1 and S2, respectively.

$$\text{proxy mechanism in Model S1}: \quad pNO_3 + h\nu \xrightarrow{150 \times j_{HNO3}} HONO \xrightarrow{j_{HONO}} NO_2$$

$$\text{proxy mechanism in Model S2}: \quad pNO_3 + h\nu \xrightarrow{150 \times j_{HNO3}} NO_2$$

To mimic the photochemical evolution of reactive nitrogen species in the typical tropospheric background and represent external cycling and its perturbation on OH photochemistry across various NO_x regimes over a large geographic area, the model was initialized with a NO_x mixing ratio of 10 ppbv, as observed in the Fort Martin station power plant plume. Concentrations of O_3 and OH were initialized at 30 ppbv and $1.7 \times 10^6 cm^{-3}$, respectively, which were typically observed in our daytime measurements. To best represent the radical chemistry for the background troposphere, an OH reactivity of approximately $5 s^{-1}$ was used for the model based on our aircraft measurements of VOCs and other species that consume OH, such as O_3, NO_x, and CO. CO, CH_4, HCHO, and CH_3CHO were found to be the top four contributors to OH reactivity in the background troposphere. To simplify the model, all measured VOCs, except HCHO and CH_3CHO, were grouped with CO to obtain an equivalent OH reactivity. The oxidative mechanism of these grouped VOCs was thus not included in our model. The photosteady state was established quickly in the model under these initial conditions. Because our focus was on the photochemical cycling of HONO and NO_2, the models were run without day-night shifts and had constant photolysis frequencies under zero solar zenith angle conditions (Table S4) to mimic the continuous 400 hr photochemical aging of the power plant plume in the background troposphere. After approximately 100 hours, the model simulation reached a stable stage. Thus, only results for the first 200 hours are shown. The model settings and initialization conditions are summarized in Tables S3 and S4.

Our model generally reproduces the observation of reactive nitrogen in various atmospheric chemical regimes. The slightly lower modeling of the $HONO/NO_y$ ratio and NO_2/NO_y ratio might be partly accounted for by measurement underestimations in NO_y species (Figs. 5 and S4). Air bubbles can deactivate the Cd columns in LPAPs, leading to potentially lower nitrate-to-nitrite conversion efficiencies; measurement underestimations in pNO_3 and HNO_3 from this phenomenon were recently estimated to reach twofold[23]. Incomplete NO_y measurements in the aircraft platform, such as measurements of other alkyl nitrates, and uncertainties in the organic nitrogen formation mechanism might be other reasons[17]. An assumed extreme case of 100% HONO yield in model S1 might be another reason, as the direct yield of NO_2 cannot be excluded[4,25].

GEOS-Chem simulation

The GEOS-Chem model (version 9-02; www.geos-chem.org) regional simulations were conducted in a one-way nested grid formulation with the native GEOS-5 Forward Processing horizontal resolution of 0.25° × 0.3125° over the North America domain (130–60° W, 10–60° N). The initial and boundary conditions were obtained through a global GEOS-Chem model simulation with a coarser resolution of 2° × 2.5° (reduced from the native GEOS-5 forward processing grid). The GEOS-Chem meteorological fields were obtained from the assimilated products of the NASA Global Modeling and Assimilation Office Goddard Earth Observing System (http://gmao.gsfc.nasa.gov/products/). The model simulations had 47 vertical layers in the atmosphere. We used a non-local planetary boundary layer mixing scheme developed by Holtslag and Boville (1993) and implemented in GEOS-Chem by Lin and McElroy (2010)[64,65]. The tropospheric chemistry mechanism was described in Parrella et al. (2012)[66]. No further updates, including external cycling, were made. Emissions of atmospheric components included anthropogenic emissions from the Emissions Database for Global Atmospheric Research (https://edgar.jrc.ec.europa.eu), biogenic emissions of volatile organic carbons from the Model of Emissions of Gases and Aerosols from Nature inventory[67], fire emissions from the Global Fire Emissions Database[68], soil NO_x emissions[69], and lightning NO_x sources[70]. The dry deposition scheme used a resistance in-series model based on Wesely (1989)[71]. The wet deposition scheme included the scavenging of soluble tracers in convective updrafts as well as the rainout and washout of soluble tracers[72]. Simulation results corresponding to the research flight track during the same period were extracted for measurement comparison.

Data availability

The field data used in this study have been deposited and are freely available in the SAS project data archive (http://data.eol.ucar.edu/master_list/?project=SAS).

Code availability

The full set of the MCM model mechanism can be extracted from the MCM website (https://mcm.york.ac.uk/MCM/) and the subset is also available from the corresponding author upon request.

References

1. Alicke, B., Platt, U. & Stutz, J. Impact of nitrous acid photolysis on the total hydroxyl radical budget during the Limitation of Oxidant Production/Pianura Padana Produzione di Ozono study in Milan. *J. Geophys. Res.-Atmos.* **107**, LOP 9-1–LOP 9-17 (2002).
2. Platt, U., Perner, D., Harris, G. W., Winer, A. M. & Pitts, J. N. Observations of Nitrous-Acid in an Urban Atmosphere by Differential Optical-Absorption. *Nature* **285**, 312–314 (1980).
3. Levy, H. 2nd. Normal atmosphere: large radical and formaldehyde concentrations predicted. *Science* **173**, 141–143 (1971).
4. Ye, C. et al. Rapid cycling of reactive nitrogen in the marine boundary layer. *Nature* **532**, 489–491 (2016).
5. Murray, L. T., Fiore, A. M., Shindell, D. T., Naik, V. & Horowitz, L. W. Large uncertainties in global hydroxyl projections tied to fate of reactive nitrogen and carbon. *Proc. Natl Acad. Sci. USA* **118**, e2115204118 (2021).

6. Whalley, L. K. et al. Atmospheric OH reactivity in central London: observations, model predictions and estimates of in situ ozone production. *Atmos. Chem. Phys.* **16**, 2109–2122 (2016).
7. Stemmler, K., Ammann, M., Donders, C., Kleffmann, J. & George, C. Photosensitized reduction of nitrogen dioxide on humic acid as a source of nitrous acid. *Nature* **440**, 195–198 (2006).
8. George, C., Strekowski, R. S., Kleffmann, J., Stemmler, K. & Ammann, M. Photoenhanced uptake of gaseous NO2 on solid organic compounds: a photochemical source of HONO? *Faraday Discuss.* **130**, 195–210 (2005).
9. Elshorbany, Y. F., Steil, B., Bruhl, C. & Lelieveld, J. Impact of HONO on global atmospheric chemistry calculated with an empirical parameterization in the EMAC model. *Atmos. Chem. Phys.* **12**, 9977–10000 (2012).
10. Han, C., Yang, W., Wu, Q., Yang, H. & Xue, X. Heterogeneous Photochemical Conversion of NO2 to HONO on the Humic Acid Surface under Simulated Sunlight. *Environ. Sci. Technol.* **50**, 5017–5023 (2016).
11. Ammann, M. et al. Heterogeneous production of nitrous acid on soot in polluted air masses. *Nature* **395**, 157–160 (1998).
12. Wong, K. W. et al. Daytime HONO vertical gradients during SHARP 2009 in Houston, TX. *Atmos. Chem. Phys.* **12**, 635–652 (2012).
13. Hendrick, F. et al. Four years of ground-based MAX-DOAS observations of HONO and NO2 in the Beijing area. *Atmos. Chem. Phys.* **14**, 765–781 (2014).
14. Chai, J. J. et al. Isotopic evidence for dominant secondary production of HONO in near-ground wildfire plumes. *Atmos. Chem. Phys.* **21**, 13077–13098 (2021).
15. Jiang, Y. et al. Sources of nitrous acid (HONO) in the upper boundary layer and lower free troposphere of the North China Plain: insights from the Mount Tai Observatory. *Atmos. Chem. Phys.* **20**, 12115–12131 (2020).
16. Oswald, R. et al. HONO emissions from soil bacteria as a major source of atmospheric reactive nitrogen. *Science* **341**, 1233–1235 (2013).
17. Peng, Q. Y. et al. Observations and Modeling of NOx Photochemistry and Fate in Fresh Wildfire Plumes. *ACS Earth Space Chem.* **5**, 2652–2667 (2021).
18. Dyson, J. E. et al. Production of HONO from NO2 uptake on illuminated TiO2 aerosol particles and following the illumination of mixed TiO2/ammonium nitrate particles. *Atmos. Chem. Phys.* **21**, 5755–5775 (2021).
19. Su, H. et al. Soil nitrite as a source of atmospheric HONO and OH radicals. *Science* **333**, 1616–1618 (2011).
20. Domine, F. & Shepson, P. B. Air-snow interactions and atmospheric chemistry. *Science* **297**, 1506–1510 (2002).
21. Romer, P. S. et al. Constraints on Aerosol Nitrate Photolysis as a Potential Source of HONO and NO (x). *Environ. Sci. Technol.* **52**, 13738–13746 (2018).
22. Reed, C. et al. Evidence for renoxification in the tropical marine boundary layer. *Atmos. Chem. Phys.* **17**, 4081–4092 (2017).
23. Zhu, Y. T. et al. An investigation into the chemistry of HONO in the marine boundary layer at Tudor Hill Marine Atmospheric Observatory in Bermuda. *Atmos. Chem. Phys.* **22**, 6327–6346 (2022).
24. Zhou, X. L. et al. Nitric acid photolysis on surfaces in low-NOx environments: Significant atmospheric implications. *Geophys. Res. Lett.* **30**, ASC 12-1–ASC 12-4 (2003).
25. Ye, C., Heard, D. E. & Whalley, L. K. Evaluation of Novel Routes for NO(x) Formation in Remote Regions. *Environ. Sci. Technol.* **51**, 7442–7449 (2017).
26. Helas, G. & Warneck, P. Background Nox Mixing Ratios in Air Masses over the North-Atlantic Ocean. *J. Geophys. Res. -Oceans* **86**, 7283–7290 (1981).
27. Grannas, A. M. et al. An overview of snow photochemistry: evidence, mechanisms and impacts. *Atmos. Chem. Phys.* **7**, 4329–4373 (2007).
28. Villena, G. et al. Nitrous acid (HONO) during polar spring in Barrow, Alaska: A net source of OH radicals? *J. Geophys. Res. -Atmos.* **116**, 1–12 (2011).
29. Zhou, X. L. et al. Snowpack photochemical production of HONO: a major source of OH in the Arctic boundary layer in springtime. *Geophys. Res. Lett.* **28**, 4087–4090 (2001).
30. Ye, C. X., Zhang, N., Gao, H. L. & Zhou, X. L. Photolysis of Particulate Nitrate as a Source of HONO and NOx. *Environ. Sci. Technol.* **51**, 6849–6856 (2017).
31. Zhou, X. L. et al. Nitric acid photolysis on forest canopy surface as a source for tropospheric nitrous acid. *Nat. Geosci.* **4**, 440–443 (2011).
32. Ye, C. X. et al. Tropospheric HONO distribution and chemistry in the southeastern US. *Atmos. Chem. Phys.* **18**, 9107–9120 (2018).
33. Ye, C., Zhang, N., Gao, H. & Zhou, X. Matrix effect on surface-catalyzed photolysis of nitric acid. *Sci. Rep.* **9**, 4351 (2019).
34. Peng, Q. Y. et al. Direct Constraints on Secondary HONO Production in Aged Wildfire Smoke From Airborne Measurements Over the Western US. *Geophys. Res. Lett.* **49**, e2022GL098704 (2022).
35. Kasibhatla, P. et al. Global impact of nitrate photolysis in sea-salt aerosol on NOx, OH, and O–3 in the marine boundary layer. *Atmos. Chem. Phys.* **18**, 11185–11203 (2018).
36. Bao, F., Li, M., Zhang, Y., Chen, C. & Zhao, J. Photochemical Aging of Beijing Urban PM(2.5): HONO Production. *Environ. Sci. Technol.* **52**, 6309–6316 (2018).
37. Baergen, A. M. & Donaldson, D. J. Photochemical renoxification of nitric acid on real urban grime. *Environ. Sci. Technol.* **47**, 815–820 (2013).
38. Andersen, S. T. et al. Extensive field evidence for the release of HONO from the photolysis of nitrate aerosols. *Sci. Adv.* **9**, eadd6266 (2023).
39. Shi, Q. et al. Laboratory Investigation of Renoxification from the Photolysis of Inorganic Particulate Nitrate. *Environ. Sci. Technol.* **55**, 854–861 (2021).
40. Lee, J. D. et al. Year-round measurements of nitrogen oxides and ozone in the tropical North Atlantic marine boundary layer. *J. Geophys. Res.-Atmos.* **114**, D21302 (2009).
41. Li, X. et al. Missing gas-phase source of HONO inferred from Zeppelin measurements in the troposphere. *Science* **344**, 292–296 (2014).
42. Pike, R. C. et al. NOx and O–3 above a tropical rainforest: an analysis with a global and box model. *Atmos. Chem. Phys.* **10**, 10607–10620 (2010).
43. Zhang, N. et al. Aircraft measurement of HONO vertical profiles over a forested region. *Geophys. Res. Lett.* **36**, L15820 (2009).
44. Neuman, J. A. et al. HONO emission and production determined from airborne measurements over the Southeast US. *J. Geophys. Res. -Atmos.* **121**, 9237–9250 (2016).
45. Travis, K. R. et al. Why do models overestimate surface ozone in the Southeast United States? *Atmos. Chem. Phys.* **16**, 13561–13577 (2016).
46. Crilley, L. R. et al. Intercomparison of nitrous acid (HONO) measurement techniques in a megacity (Beijing). *Atmos. Meas. Tech.* **12**, 6449–6463 (2019).
47. Chen, Q. J. et al. HONO, Particulate Nitrite, and Snow Nitrite at a Midlatitude Urban Site during Wintertime. *ACS Earth Space Chem.* **3**, 811–822 (2019).
48. Wang, L. et al. HONO and its potential source particulate nitrite at an urban site in North China during the cold season. *Sci. Total Environ.* **538**, 93–101 (2015).
49. Fuchs, H. et al. Intercomparison of measurements of NO2 concentrations in the atmosphere simulation chamber SAPHIR during the NO3Comp campaign. *Atmos. Meas. Tech.* **3**, 21–37 (2010).
50. Honrath, R. E. et al. Evidence of NOx production within or upon ice particles in the Greenland snowpack. *Geophys. Res. Lett.* **26**, 695–698 (1999).

51. Taraborrelli, D. et al. Hydroxyl radical buffered by isoprene oxidation over tropical forests. *Nat. Geosci.* **5**, 190–193 (2012).
52. Lelieveld, J. et al. Atmospheric oxidation capacity sustained by a tropical forest. *Nature* **452**, 737–740 (2008).
53. Akimoto, H. & Tanimoto, H. Review of Comprehensive Measurements of Speciated NOy and its Chemistry: Need for Quantifying the Role of Heterogeneous Processes of HNO3 and HONO. *Aerosol Air Qual. Res.* **21**, 200395 (2021).
54. Shah, V. R. et al. Nitrogen oxides in the free troposphere: implications for tropospheric oxidants and the interpretation of satellite NO2 measurements. *Atmos. Chem. Phys.* **23**, 1227–1257 (2023).
55. Ridley, B. et al. Florida thunderstorms: A faucet of reactive nitrogen to the upper troposphere. *J. Geophys. Res. -Atmos.* **109**, 1–19 (2004).
56. Griffin, R. J., Beckman, P. J., Talbot, R. W., Sive, B. C. & Varner, R. K. Deviations from ozone photostationary state during the International Consortium for Atmospheric Research on Transport and Transformation 2004 campaign: Use of measurements and photochemical modeling to assess potential causes. *J. Geophys. Res.-Atmos.* **112**, D10S07 (2007).
57. Huang, G., Zhou, X. L., Deng, G. H., Qiao, H. C. & Civerolo, K. Measurements of atmospheric nitrous acid and nitric acid. *Atmos. Environ.* **36**, 2225–2235 (2002).
58. Kulkarni, P., Baron, P. A. & Willeke, K. *Aerosol Measurement: Principles, Techniques, and Applications*. (John Wiley & Sons, Inc., Hoboken), (2011).
59. de Gouw, J. & Warneke, C. Measurements of volatile organic compounds in the earth's atmosphere using proton-transfer-reaction mass spectrometry. *Mass Spectrom. Rev.* **26**, 223–257 (2007).
60. Hornbrook, R. S. et al. Measurements of tropospheric HO2 and RO2 by oxygen dilution modulation and chemical ionization mass spectrometry. *Atmos. Meas. Tech.* **4**, 735–756 (2011).
61. Shetter, R. E., Cinquini, L., Lefer, B. L., Hall, S. R. & Madronich, S. Comparison of airborne measured and calculated spectral actinic flux and derived photolysis frequencies during the PEM Tropics B mission. *J. Geophys. Res.-Atmos.* **108**, PEM 6-1–PEM 6-8 (2002).
62. Stemmler, K. et al. Light induced conversion of nitrogen dioxide into nitrous acid on submicron humic acid aerosol. *Atmos. Chem. Phys.* **7**, 4237–4248 (2007).
63. Carlton, A. G. et al. SYNTHESIS OF THE SOUTHEAST ATMOSPHERE STUDIES: Investigating Fundamental Atmospheric Chemistry Questions. *Bull. Am. Meteorol. Soc.* **99**, 547–567 (2018).
64. Holtslag, A. A. M. & Boville, B. A. Local Versus Nonlocal Boundary-Layer Diffusion in a Global Climate Model. *J. Clim.* **6**, 1825–1842 (1993).
65. Lin, J. T. & McElroy, M. B. Impacts of boundary layer mixing on pollutant vertical profiles in the lower troposphere: Implications to satellite remote sensing. *Atmos. Environ.* **44**, 1726–1739 (2010).
66. Parrella, J. P. et al. Tropospheric bromine chemistry: implications for present and pre-industrial ozone and mercury. *Atmos. Chem. Phys.* **12**, 6723–6740 (2012).
67. Guenther, A. B. et al. The Model of Emissions of Gases and Aerosols from Nature version 2.1 (MEGAN2.1): an extended and updated framework for modeling biogenic emissions. *Geosci. Model Dev.* **5**, 1471–1492 (2012).
68. van der Werf, G. R. et al. Global fire emissions and the contribution of deforestation, savanna, forest, agricultural, and peat fires (1997–2009). *Atmos. Chem. Phys.* **10**, 11707–11735 (2010).
69. Hudman, R. C. et al. Surface and lightning sources of nitrogen oxides over the United States: Magnitudes, chemical evolution, and outflow. *J. Geophys. Res.-Atmos.* **112**, D12S05 (2007).
70. Murray, L. T., Jacob, D. J., Logan, J. A., Hudman, R. C. & Koshak, W. J. Optimized regional and interannual variability of lightning in a global chemical transport model constrained by LIS/OTD satellite data. *J. Geophys. Res.-Atmos.* **117**, D20307 (2012).
71. Wesely, M. L. Parameterization of Surface Resistances to Gaseous Dry Deposition in Regional-Scale Numerical-Models. *Atmos. Environ.* **23**, 1293–1304 (1989).
72. Liu, H. Y., Jacob, D. J., Bey, I. & Yantosca, R. M. Constraints from Pb-210 and Be-7 on wet deposition and transport in a global three-dimensional chemical tracer model driven by assimilated meteorological fields. *J. Geophys. Res. -Atmos.* **106**, 12109–12128 (2001).

Acknowledgements

This analysis and model work is supported by the National Natural Science Foundation of China (grants 41875151, C.Y.). We acknowledge the U.S. National Natural Science Foundation (grants AGS–1216166 and AGS –1826989, X.Z.) and members of the SAS project for supporting and providing the field measurements. We really appreciate Xueling Meng for her kind help in preparing Fig. 1.

Author contributions

C.Y. interpreted the data and wrote the manuscript with revision advice from X.Z., J.W., C.Z., R.W.M., C.C., R.L.M., T.C., R.S.H., J.O., E.C.A., J.H., S.H., K.U., A.W., J.S., T.K., J.N.S. and A.G., Y.Z. prepared the figures. Y.W. performed MCM model calculation. S.S. performed the GEOS-Chem simulation.

Competing interests

The authors declare no competing interests.

Additional information

Supplementary information The online version contains supplementary material available at https://doi.org/10.1038/s41467-023-43866-z.

Correspondence and requests for materials should be addressed to Chunxiang Ye.

Peer review information *Nature Communications* thanks the anonymous reviewer(s) for their contribution to the peer review of this work. A peer review file is available.